

Article

Energy Characteristics and Internal Flow Field Analysis of Centrifugal Prefabricated Pumping Station with Two Pumps in Operation

Chuanliu Xie ^{1,*}, Zhenyang Yuan ¹, Andong Feng ¹, Zhaojun Wang ² and Liming Wu ²¹ College of Engineering, Anhui Agricultural University, Hefei 230036, China² Suqian Branch of Jiangsu Water Source Company of South to North Water Diversion, Suqian 223800, China

* Correspondence: xcltg@ahau.edu.cn

Abstract: In order to study the hydraulic performance and internal flow field of dual pumps in centrifugal prefabricated pumping station under operation conditions, this paper carried out a numerical calculation based on CFD software for dual pumps in a centrifugal prefabricated pumping station under different flow conditions and verified the internal flow field through test. The results show that the efficiency of centrifugal prefabricated pumping station under design conditions ($Q_d = 33.93 \text{ m}^3/\text{h}$) is 63.96%, the head is 8.66 m, the head at the starting point of the saddle area is 10.50 m, which is 1.21 times of the designed head. The efficiency of the high-efficiency zone of the prefabricated pump station is 58.0~63.0%, and the corresponding flow range is $0.62Q_d \sim 1.41Q_d$ ($21.0 \sim 48.0 \text{ m}^3/\text{h}$). The uniformity of the inlet flow rate of impeller of pump 1 is 74.70%, and that of pump 2 is 75.57%. The flow fields of water pumps on both sides are inconsistent. The results of the flow field indicate that there are severe back flow phenomena at the prefabricated bucket intake, more back flow in the bucket, and many eddies on the side wall. With the increase in flow rate, the eddy structure at the intake expands continuously and moves towards the center area, which has a negative impact on the flow field in the center area. The research results of this paper can provide a theoretical reference for the research and operation of the same type of prefabricated pumping stations.

Keywords: prefabricated pumping station; centrifugal pump; energy characteristics; internal flow field; test



Citation: Xie, C.; Yuan, Z.; Feng, A.; Wang, Z.; Wu, L. Energy Characteristics and Internal Flow Field Analysis of Centrifugal Prefabricated Pumping Station with Two Pumps in Operation. *Water* **2022**, *14*, 2705. <https://doi.org/10.3390/w14172705>

Academic Editors: Changliang Ye, Xijie Song and Ran Tao

Received: 1 August 2022

Accepted: 29 August 2022

Published: 30 August 2022

Publisher's Note: MDPI stays neutral with regard to jurisdictional claims in published maps and institutional affiliations.



Copyright: © 2022 by the authors. Licensee MDPI, Basel, Switzerland. This article is an open access article distributed under the terms and conditions of the Creative Commons Attribution (CC BY) license (<https://creativecommons.org/licenses/by/4.0/>).

1. Introduction

With the worsening weather in recent years, some areas are often damaged by flood disasters, and the role of pumping stations is becoming increasingly prominent. Traditional pumping stations are mainly concrete pumping stations, which are costly, have a long construction period, and consume a lot of manpower and material resources. They cannot be moved after construction [1]. In this context, prefabricated pumping stations have gradually developed. Prefabricated pumping stations originated in Europe at the earliest. They are small and movable new drainage and irrigation equipment that combine all the components of the pumping stations into one unit. Compared with the traditional concrete pumping station, the prefabricated pumping station has the advantages of simple installation, short construction period, small area, good saving of land resources, and good economic benefits. A prefabricated pumping station is a power water conveyance device that integrates pumps, cylinders, pipes, and other components. At present, the research on prefabricated pumping stations is mostly focused on engineering applications. The flow pattern in the prefabricated pumping station is quite complex, and the bad flow pattern often affects the stable operation of the pumping station, causing cavitation and vibration of the pump and even damaging parts of the pump in serious cases. However, there is little research on the operation capacity and internal flow field of the prefabricated pumping station. The hydraulic performance and internal flow characteristics of the prefabricated

pumping station are not clear, which makes it impossible to operate efficiently, stably, and safely. Therefore, it is necessary to study the prefabricated pumping station in depth.

Some scholars have carried out some research on the prefabricated pumping station; for example, related scholars pointed out that integrated prefabricated pumping station has great advantages in volume, service efficiency, etc. [2], analyzed the strength of integrated prefabricated pumping station cylinder [3], analyzed the sedimentation characteristics of solids when multiphase flow in integrated prefabricated pumping station [4,5], and analyzed the installation parameters of pumps in prefabricated pumping station [6]. There are few studies on the integrated pumping station. The research focuses on engineering application, structural design, and deposition of multiphase flow solids. There is little research on its hydraulic performance and internal flow characteristics. Studies have shown the advantages of using CFD methods for centrifugal pump characteristics and flow field studies; for example, related scholars have used CFD methods to analyze the energy characteristics of centrifugal pumps [7,8] and the pressure, velocity, and streamline the distribution of centrifugal pumps [9], and the literature [10] shows that the energy characteristics of centrifugal pumps can be studied using the SST $k-\omega$ turbulence model. Related scholars have combined numerical calculations with experiments to analyze and discuss the pump performance and internal flow patterns; for example, some scholars have compared the numerical calculation results with experimental data for multiple working conditions [11], studied the effect of cutouts on the guide vane on the pump performance and internal flow [12], revealed the performance and internal flow characteristics of multi-stage single suction centrifugal pumps, analyzed in detail the internal flow and pressure field of centrifugal pumps [13], and analyzed the effect of impeller vane number and angle on the performance of centrifugal pumps [14].

In this paper, considering the influence of structural components on the internal flow field, the local dimensions of structural components are not simplified, and numerical calculations and experimental analysis are used for the study with a view to gaining insight into the hydraulic performance and internal flow characteristics of prefabricated pumping stations in actual operation, revealing the undesirable flow patterns inside prefabricated pumping stations, and providing theoretical guidance for the optimal design and operation of prefabricated pumping stations. The research in this paper has certain academic significance and engineering application value.

2. Three-Dimensional Modeling and Numerical Calculation Setup

2.1. Calculation Model

In this paper, Solidworks software [15] is used to build the three-dimensional model of the whole pumping station. When modeling, the influence of the structural components such as motor, pipe, and flange in the pumping station on the water flow is considered. The overall height of the cylinder is $L = 1$ m, the diameter of the cylinder is $D = 1$ m, and the diameter of the intake and outlet is $R = 100$ mm. The pump used in this paper is a submerged centrifugal pump with a diameter of impeller $d = 100$ mm, number of vanes of 3 pieces, and speed $n = 2900$ r/min. The three-dimensional model is as shown in the Figure 1.

2.2. Meshing

In this paper, the water body parts inside the structural components are extracted by SolidWorks software, and the three-dimensional model is meshed in Mesh software. The mesh calculation area mainly includes the inlet section, prefabricated barrel, impeller, guide vane, and outlet section. Because the fluid excises more structural components and is more complex, this paper uses non-structural tetrahedral mesh for mesh division, and the mesh is better adapted [16–18]. The fluid calculation mesh of the centrifugal prefabricated pumping station is shown in Figure 2.

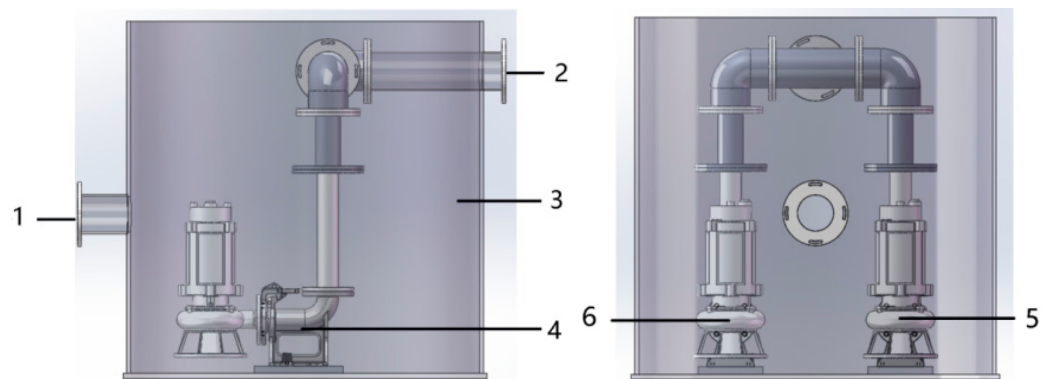


Figure 1. General assembly drawing of three-dimensional model of centrifugal prefabricated pumping station. 1. Inlet; 2. outlet; 3. round prefabricated barrels; 4. couplers; 5. submersible centrifugal pump 1; 6. submersible centrifugal pump 2.

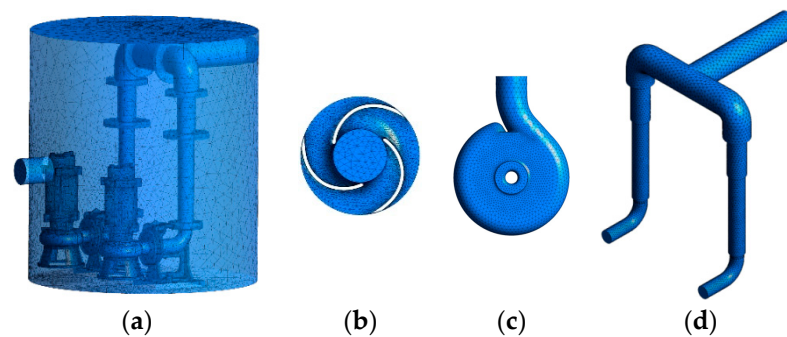


Figure 2. Grid of each calculation domain. (a) Prefabricated barrel grid; (b) impeller grid; (c) worm gear grid; (d) outlet section grid.

In this paper, seven scenarios with different numbers of meshes under the design condition ($Q_d = 33.93 \text{ m}^3/\text{h}$) are selected for the numerical calculation of the centrifugal prefabricated pumping station, and the efficiency of the centrifugal prefabricated pumping station is used as the evaluation index. It can be seen from Figure 3 that when the number of grids is between 0.9 million and 3 million, the efficiency changes greatly and is unstable. When the number of grids reaches 3.2 million, the efficiency curve basically remains unchanged, indicating that the increase in the number of grids has little impact on the calculation results [19]. Considering the computer performance and the accuracy of the calculation results, this paper selects 3.2 million grids for numerical calculation.

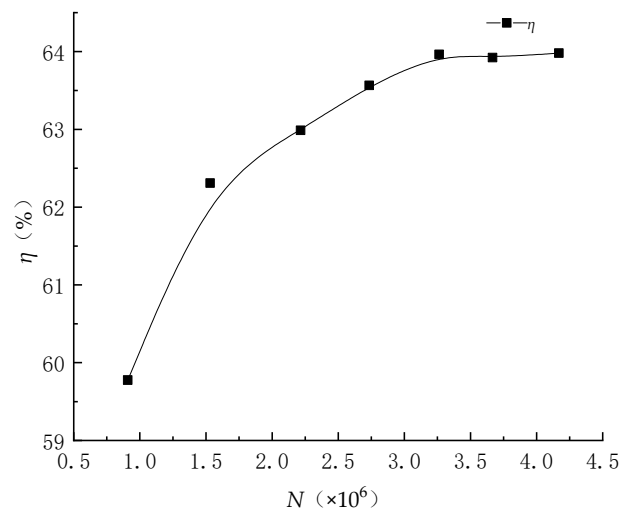


Figure 3. Grid irrelevance analysis diagram.

2.3. Boundary Conditions and Turbulence Model

The inlet of a centrifugal prefabricated pumping station is on the side of the prefabricated barrel, on the same level as the outlet. The condition for the inlet is set to Total Pressure, and the pressure magnitude is set to one atmosphere. The outlet is the outlet of the centrifugal prefabricated pumping station, and the outlet condition is set to Normal Speed. The solid wall is set to a no-slip boundary condition [20], the fluid has zero velocity near the wall, and the effect of wall roughness is not taken into account. The surface wall condition of the impeller is also set to the Rotating wall, and the surface wall condition of the cylinder, worm casing, and outlet section is set to the Static wall, applying the boundary no-slip boundary condition. In this paper, the two pumps are arranged symmetrically on the central axis of the cylinder, two rotation axes are set for the numerical calculation, the vertical direction of the impeller centers of pump 1 and pump 2 are used to determine the respective rotation axes, the coordinate positions of pump 1 rotation axis are (0.235, 0.1, 0.265), and pump 2 rotation axis coordinates are (−0.235, 0.1, −0.265).

In the calculation area, the calculation area of the inlet section, the cylinder, the worm housing, and the outlet section are set to the static domain, and the calculation area of the impeller is set to the rotational domain. In this paper, the Frozen Rotor interfacing model is used as the dynamic and static interfacing model for the fluid connection between the impeller and the worm gear. The numerical calculation of the centrifugal prefabricated pumping station uses the Reynolds time-averaged N-S equation, and the turbulence model uses the SST $k-\omega$ [21,22] turbulence model, which absorbs the advantages of the standard $k-\varepsilon$ model and the standard $k-\omega$ model, and adopts the automatic function at the boundary layer, which can better capture the flow at the boundary layer. The diffusion term and pressure gradient are represented by the finite volume method based on finite elements, and the convective term is in the High-Resolution Scheme. In the calculation, the pressure of the flow field is P ; the velocities in the x , y , and z directions are u , v , and w ; the convergence conditions of the turbulent kinetic energy k equation and the dissipation rate ε are set to 10^{-5} , and in principle, the smaller the residuals are, the better.

2.4. Calculation Formula

2.4.1. Control Equations

Turbulence control equation (N-S equation):

$$\frac{\partial(\rho u_i)}{\partial t} + \frac{\partial(\rho u_i u_j)}{\partial x_j} = -\frac{\partial P}{\partial x_i} + \left[\mu \left(\frac{\partial u_i}{\partial x_j} + \frac{\partial u_j}{\partial x_i} \right) \right] + F_i \quad (1)$$

where t is time (s); ρ is fluid density (kg/m^3); x_i and x_j are spatial coordinates; u_i and u_j are the velocity components of the fluid parallel to the corresponding axes x_i and x_j , respectively, and F_i is the volume force component in the i -direction; μ is the fluid dynamic viscosity coefficient; P is the pressure (Pa).

The transport equation of the SST $k-\omega$ turbulence model can be expressed as:

$$\frac{\partial(\rho k)}{\partial t} + \frac{\partial(\rho k u_i)}{\partial x_i} = \frac{\partial}{\partial x_j} \left[\left(\mu + \frac{\mu_t}{\sigma_k} \right) \frac{\partial k}{\partial x_j} \right] + G_k - Y_k + S_k \quad (2)$$

$$\frac{\partial(\rho \omega)}{\partial t} + \frac{\partial(\rho \omega u_i)}{\partial x_i} = \frac{\partial}{\partial x_j} \left[\left(\mu + \frac{\mu_t}{\sigma_\omega} \right) \frac{\partial \omega}{\partial x_j} \right] + G_\omega - Y_\omega + S_\omega + D_\omega \quad (3)$$

where G_k , G_ω is the generating term of the equation; Y_k , Y_ω is the generating term of the diffusive action; S_k , S_ω is the user-defined source term; D_ω is the term generated by the orthogonal divergence; k is the turbulent kinetic energy; ω is the turbulent special dissipation; μ_t is turbulent dynamic viscosity coefficient.

2.4.2. Hydraulic Performance Prediction

Centrifugal prefabricated pumping station head, expressed by the following equation [23,24]:

$$H_{net} = \left(\frac{\int P_2 u_t ds}{\rho Q g} + H_2 + \frac{\int u_{t2}^2 ds}{2Qg} \right) - \left(\frac{\int P_1 u_t ds}{\rho Q g} + H_1 + \frac{\int u_{t1}^2 ds}{2Qg} \right) \quad (4)$$

where the first term on the right side of the equation is the total pressure at the outlet section of the prefabricated barrel, and the second term is the total pressure at the inlet section of the prefabricated barrel. Q —flow rate, m^3/s ; H_1, H_2 —prefabricated barrel inlet and outlet section elevation, m.

s_1, s_2 —prefabricated barrel inlet and outlet section area; u_1, u_2 —prefabricated barrel inlet and outlet flow velocity at each point, m/s; u_{t1}, u_{t2} —prefabricated barrel inlet and outlet section flow velocity normal component at each point, m/s.

P_1, P_2 —prefabricated barrel inlet and outlet section at each point of the static pressure, Pa; g —gravitational acceleration, m/s^2 .

The efficiency of centrifugal prefabricated pumping stations is [25–27]:

$$\eta = \frac{\rho g Q H_{net}}{N_1 + N_2} \quad (5)$$

where N_1 —shaft power of pump 1, N_2 —shaft power of pump 2.

The shaft power of the centrifugal prefabricated pumping station is [28,29]:

$$N = \frac{\pi}{30} T n \quad (6)$$

where T —torque, N —m; n —rotational speed, r/min.

2.4.3. Uniformity of Flow Velocity Distribution

The uniformity of axial velocity distribution V_{zu} of the section at the impeller inlet reflects the water inlet quality of the impeller, and the closer V_{zu} is to 100%, the more uniform the water inlet of the impeller is, and its calculation formula is as follows [30]:

$$V_{zu} = \left\{ 1 - \frac{1}{\bar{v}_a} \sqrt{\frac{\sum_{i=1}^n (v_{ai} - \bar{v}_a)^2}{n}} \right\} \times 100\% \quad (7)$$

where V_{zu} —uniformity of flow velocity distribution at impeller inlet, %; V_a —arithmetic mean of axial flow velocity at impeller inlet; V_{ai} —axial velocity of each calculation unit at impeller inlet, m/s; n —number of calculation units at impeller inlet.

3. Energy and Internal Flow Characteristics Analysis

In this paper, the numerical calculation results under different flow conditions are extracted to analyze the flow field characteristics inside the centrifugal prefabricated pumping station. The numerical calculations are divided into 12 flow conditions, which are 11.31 m^3/h ($0.33Q_d$), 16.96 m^3/h ($0.50Q_d$), 22.62 m^3/h ($0.67Q_d$), 28.27 m^3/h ($0.83Q_d$), 33.93 m^3/h ($1.00Q_d$), 39.58 m^3/h ($1.17Q_d$), 45.24 m^3/h ($1.33Q_d$), 50.89 m^3/h ($1.50Q_d$), 56.55 m^3/h ($1.67Q_d$), 62.20 m^3/h ($1.83Q_d$), 67.86 m^3/h ($2.00Q_d$), 73.51 m^3/h ($2.17Q_d$), and 79.17 m^3/h ($2.33Q_d$); design flow working condition is $Q_d = 33.93 m^3/h$.

3.1. Energy Characteristics Analysis

The numerical calculation results of the centrifugal prefabricated pumping station at different flow rates are extracted, and the head and efficiency of centrifugal prefabricated pumping station are calculated by Equations (4)–(6), followed by drawing the energy char-

acteristic curve of the centrifugal prefabricated pumping station. The energy characteristics are shown in Table 1 and Figure 4.

Table 1. Energy characteristics data table.

Flow Rate Q (m^3/h)	Head H (m)	Efficiency η (%)
11.31 ($0.33Q_d$)	10.50	45.05
16.96 ($0.50Q_d$)	10.33	55.28
22.62 ($0.67Q_d$)	9.91	59.77
28.27 ($0.83Q_d$)	9.39	63.22
33.93 ($1.00Q_d$)	8.66	63.96
39.58 ($1.17Q_d$)	7.77	61.78
45.24 ($1.33Q_d$)	6.84	60.36
50.89 ($1.50Q_d$)	5.91	57.54
56.55 ($1.67Q_d$)	4.93	53.17
62.20 ($1.83Q_d$)	3.94	47.15
67.86 ($2.00Q_d$)	2.92	39.18
73.51 ($2.17Q_d$)	1.90	28.97
79.17 ($2.33Q_d$)	0.57	9.98

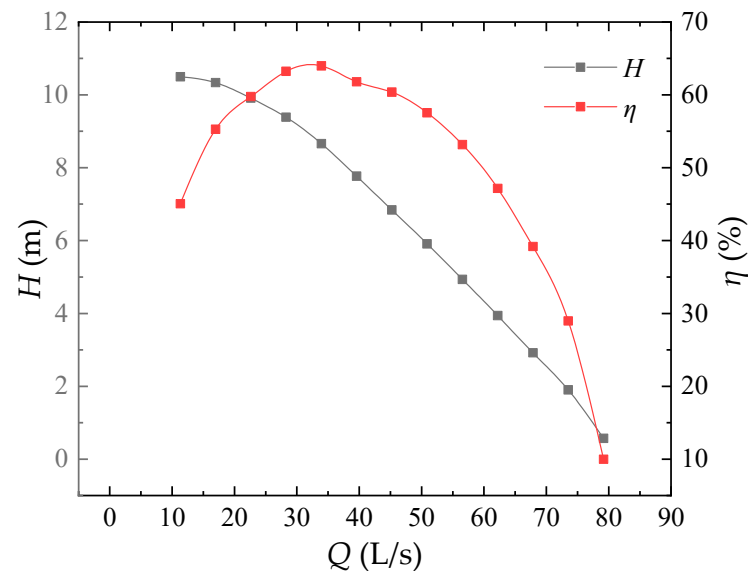


Figure 4. Energy characteristic curve at different flow rates.

The calculation results of the energy characteristics of the centrifugal prefabricated pumping station show that the efficiency of the prefabricated pumping station increases with the flow rate under the small flow rate condition ($Q = 11.31\sim 33.93 \text{ m}^3/\text{h}$), and at the flow condition $0.33Q_d$ ($Q = 11.31 \text{ m}^3/\text{h}$), the centrifugal prefabricated pumping station enters the flow instability condition (saddle zone effect area), and this phenomenon can be obviously found through the head, the head increases less from $0.50Q_d$ to $0.33Q_d$, and the slope of growth here is close to 0 from the head curve and reaches the maximum value at the design condition ($Q_d = 33.93 \text{ m}^3/\text{h}$) with the maximum efficiency value of 63.96% and the head is 8.66 m. The head at the starting point of the saddle area is 10.50 m, which is 1.21 times the design head, indicating that the operable head range for small flow is small and the operable head range for large flow is wide. Under the high flow rate condition ($Q = 33.93\sim 79.17 \text{ m}^3/\text{h}$), the efficiency decreases gradually with the increase in flow rate. The slope of the efficiency curve change increases with increasing flow rate. When the flow rate is between $21.0\sim 48.0 \text{ m}^3/\text{h}$, the prefabricated pumping station is in the high-efficiency zone (the high-efficiency zone is defined as the range of flows where the efficiency of the optimal efficiency point decreases by 5%); at this time, the pumping station device efficiency is around 58.0~63.0%. The head curve of the prefabricated pumping station

gradually decreases with the increase in flow, from 10.50 m to 0.57 m, and the efficiency curve is parabolic with the increase in flow; the head curve is approximately straight with a small change in slope.

Based on the post-processing of the numerical calculation results, the uniformity of flow velocity at the impeller inlet of pump 1 and pump 2 is calculated by Equation (7). The uniformity of flow rate is shown in Table 2 and Figure 5.

Table 2. Uniformity of impeller inlet flow rate at different flow rates.

Flow Rate Q (m^3/h)	Water Pump 1 Impeller Inlet Flow Rate Uniformity (%)	Water Pump 2 Impeller Inlet Flow Rate Uniformity (%)
11.31 ($0.33Q_d$)	68.55	66.05
16.96 ($0.50Q_d$)	70.55	73.03
22.62 ($0.67Q_d$)	73.93	74.74
28.27 ($0.83Q_d$)	74.59	75.40
33.93 ($1.00Q_d$)	74.70	75.57
39.58 ($1.17Q_d$)	74.61	75.52
45.24 ($1.33Q_d$)	74.65	75.55
50.89 ($1.50Q_d$)	74.70	75.61
56.55 ($1.67Q_d$)	74.74	75.66
62.20 ($1.83Q_d$)	74.77	75.70
67.86 ($2.00Q_d$)	74.79	75.72
73.51 ($2.17Q_d$)	74.79	75.70
79.17 ($2.33Q_d$)	74.78	75.67

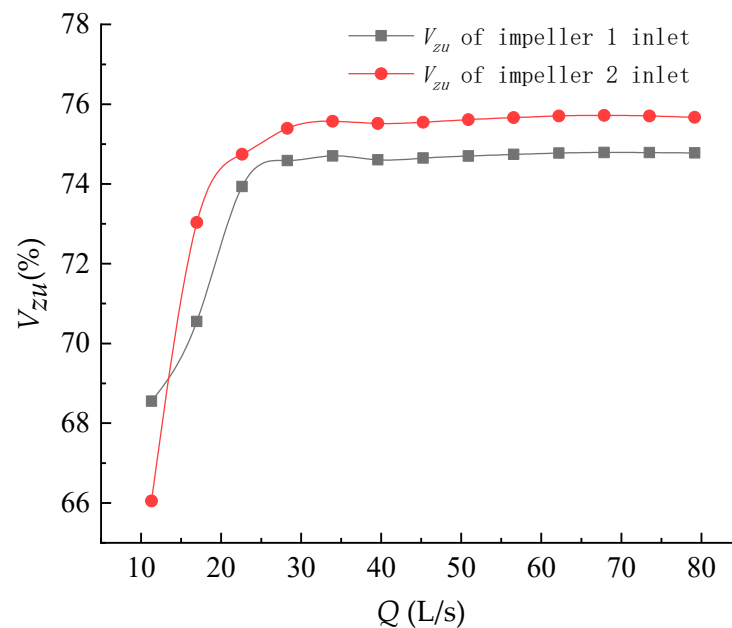


Figure 5. Uniformity of impeller inlet flow rate under different working conditions.

As can be seen from Figure 5, the variation pattern of flow uniformity with increasing flow rate at the impeller inlet of pump 1 and pump 2 is essentially the same. Under the small flow rate condition, the uniformity of flow velocity at the impeller inlet increases with the increase in flow rate, and when the flow rate reaches $0.83Q_d$ ($Q = 28.27 \text{ m}^3/\text{h}$), the uniformity of flow velocity at the impeller inlet remains basically the same with the increase in flow rate. Overall, the uniformity of flow velocity at the impeller inlet of pump 2 is greater than that of pump 1; at the design working condition ($Q_d = 33.93 \text{ m}^3/\text{h}$), the uniformity of flow velocity at the impeller inlet of pump 1 is 74.70%, and that of pump 2 is 75.57%, with a difference of 0.87%, which is caused by the different uniformity of flow velocity at the impellers of pump 1 and pump 2 due to bias flow. When the flow condition

is less than $0.83Q_d$ ($Q = 28.27 \text{ m}^3/\text{h}$), the uniformity of flow velocity at the impeller inlet decreases significantly, which indicates that the unevenness of the flow pattern inside the prefabricated barrel of the centrifugal prefabricated pumping station increases at this time and cannot provide a better impeller inlet water flow pattern.

3.2. Analysis of Internal Flow Characteristics

In the numerical calculation results of the centrifugal prefabricated pumping station, six working conditions of $0.33Q_d$, $0.67Q_d$, $1.00Q_d$, $1.33Q_d$, $1.67Q_d$, and $2.00Q_d$ are selected for the analysis of the flow field inside the prefabricated pumping station, and in order to better depict the flow field inside the prefabricated pumping station, four characteristic sections as shown in Figure 6 are selected for analysis in this paper. The A1 section is the horizontal cross section at the impeller inlet of the submersible centrifugal pump, A2 is the cross section at the center of the precast barrel inlet, A3 is the horizontal cross section at the highest liquid level of the precast barrel, and A4 is the vertical cross section at the center of the precast barrel.

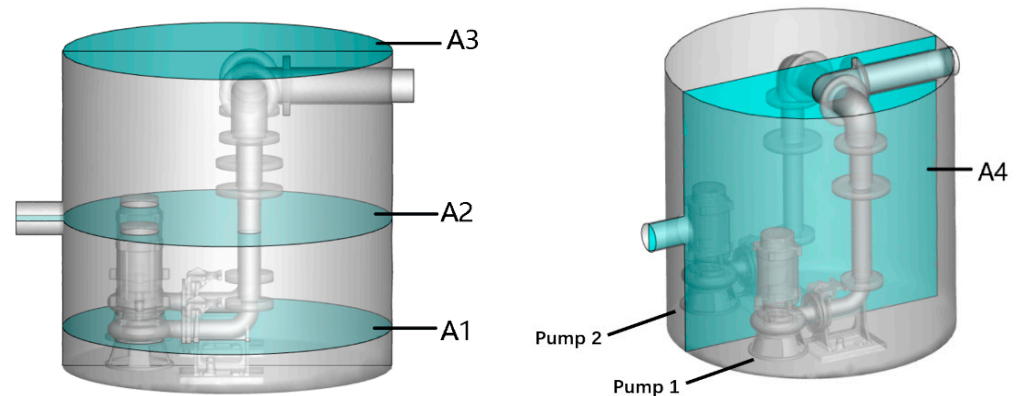


Figure 6. Schematic diagram of centrifugal prefabricated pumping station cross-section.

The velocity and streamline distributions of A1–A4 sections of centrifugal prefabricated pumping stations at $0.33Q_d$, $0.67Q_d$, $1.00Q_d$, $1.33Q_d$, $1.67Q_d$, and $2.00Q_d$ flow conditions are shown below.

Cross-section A1 flow velocity and streamline distribution is shown in Figure 7. It can be seen from Figure 7 that in the small flow conditions, the prefabricated barrel inlet side flow velocity is less than the outlet side, the impeller inlet flow velocity distribution is also uneven, the flow velocity alternates between multiple velocity classes at the impeller inlet, and there is a flow stratification effect, pump 1 and pump 2 in the middle of the water flow streamlines parallel to each other, in the prefabricated barrel along the water flow direction to see the left and right sides of the wall have vortex, and near the pump 2 vortex area is larger than near the pump 1, the coupler waterward surface on both sides of the vortex also exists, the vortex at the wall is mainly caused by the backflow of the water impacting to the back wall of the prefabricated barrel, and the backflow at the coupler is caused by the local structural features blocking the water. Under the high flow condition, the flow velocity at the impeller inlet is distributed periodically, the flow velocity distribution in the prefabricated barrel is more dispersed, the streamline is disorderly, the vortex area on both sides of the prefabricated barrel wall increases compared with the low flow condition, and the area of the vortex area for flow conditions is about twice as large as for small flow conditions.

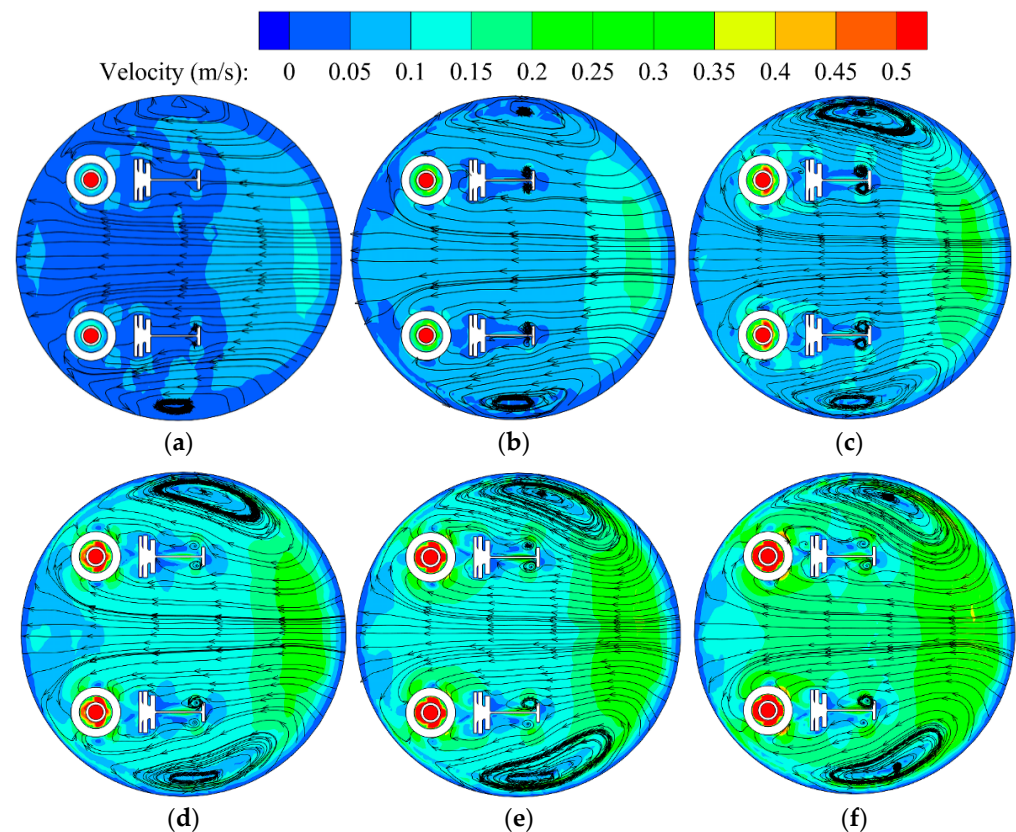


Figure 7. Cross-section A1 flow velocity and streamline distribution. (a) $0.33Q_d$, (b) $0.67Q_d$, (c) $1.00Q_d$, (d) $1.33Q_d$, (e) $1.67Q_d$, and (f) $2.00Q_d$.

Cross-section A2 flow velocity and streamline distribution is shown in Figure 8. It can be obtained from Figure 8 that the inlet is a high-speed water flow area, which is fan-shaped diffusion near the inlet of the prefabricated barrel, and the flow velocity decreases in a gradient, with the increase in the flow rate, the speed at the inlet is accelerated, and the fan-shaped diffusion area becomes larger. There are vortices on both sides of the inlet and both sides of the barrel wall, and the vortices on both sides of the inlet gradually move to the center of the prefabricated barrel with the increase in flow, and the streamlines in the center of the prefabricated barrel are parallel, and there are streamlines intersecting at pump 1 and pump 2, and the distribution of streamlines is more disorderly. Analyzed from the change in working conditions, the vortices at the inlet and sidewall both increased with the increase in flow rate. Analyzed from the position, the vortex on both sides of the inlet has basically the same area compared to each other, indicating that the bias flow does not affect the upstream flow pattern, so the symmetry is better. The area of vortex area near pump 2 is larger than that near pump 1, indicating that there is an obvious bias flow inside the prefabricated barrel.

Cross-section A3 flow velocity and streamline distribution is shown in Figure 9. It can be obtained from Figure 9 that there is a low-velocity zone at the side wall of the precast barrel wall, which is mainly due to the side wall effect, and there are three low-velocity zones in the center of the precast barrel, which is mainly due to the existence of flanges in these three places (as shown in Figure 6). There are vortices on both walls of the precast barrel, the area of the vortex region is small compared to the A1 and A2 cross sections. Analyzed in terms of the change in working conditions, and the area of the vortex zone increases with the increase in the flow rate. With the increase in flow rate, the velocity distribution in the prefabricated barrel changed obviously, producing a crescent-shaped high-speed zone on the inlet side and multiple irregular high-speed zones on the outlet side, and the streamline in the prefabricated barrel was disordered. When analyzed in

terms of location, the area of the vortex zone near pump 2 is still larger than that near pump 1, which is also caused by the bias flow effect in the prefabricated barrel.

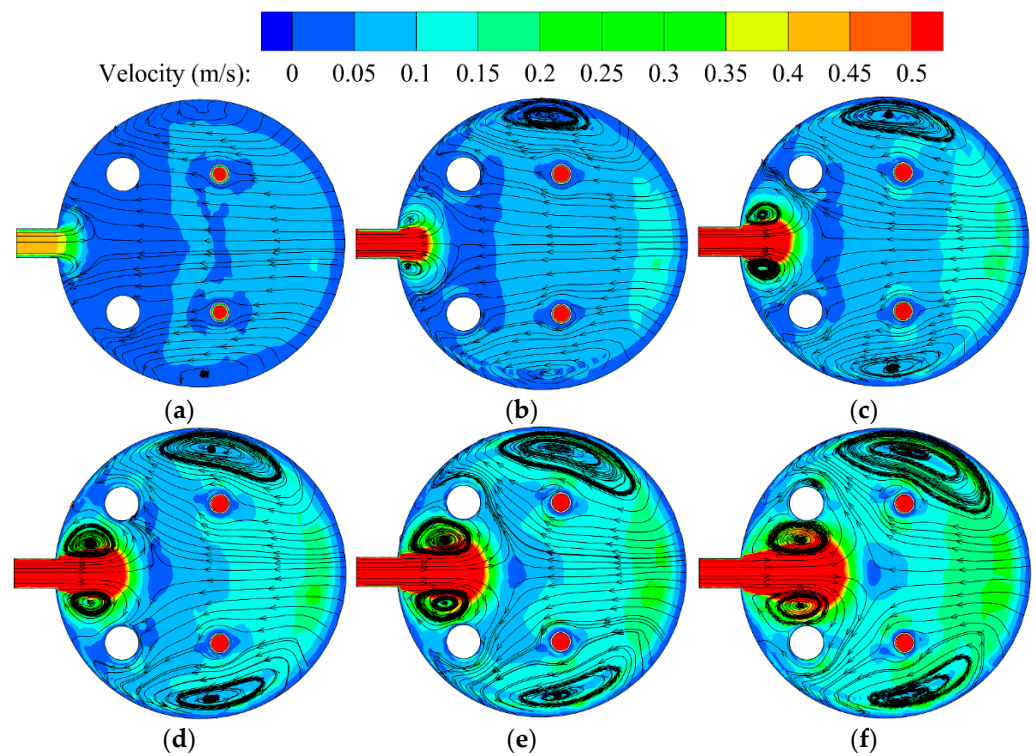


Figure 8. Cross-section A2 flow velocity and streamline distribution. (a) $0.33Q_d$, (b) $0.67Q_d$, (c) $1.00Q_d$, (d) $1.33Q_d$, (e) $1.67Q_d$, and (f) $2.00Q_d$.

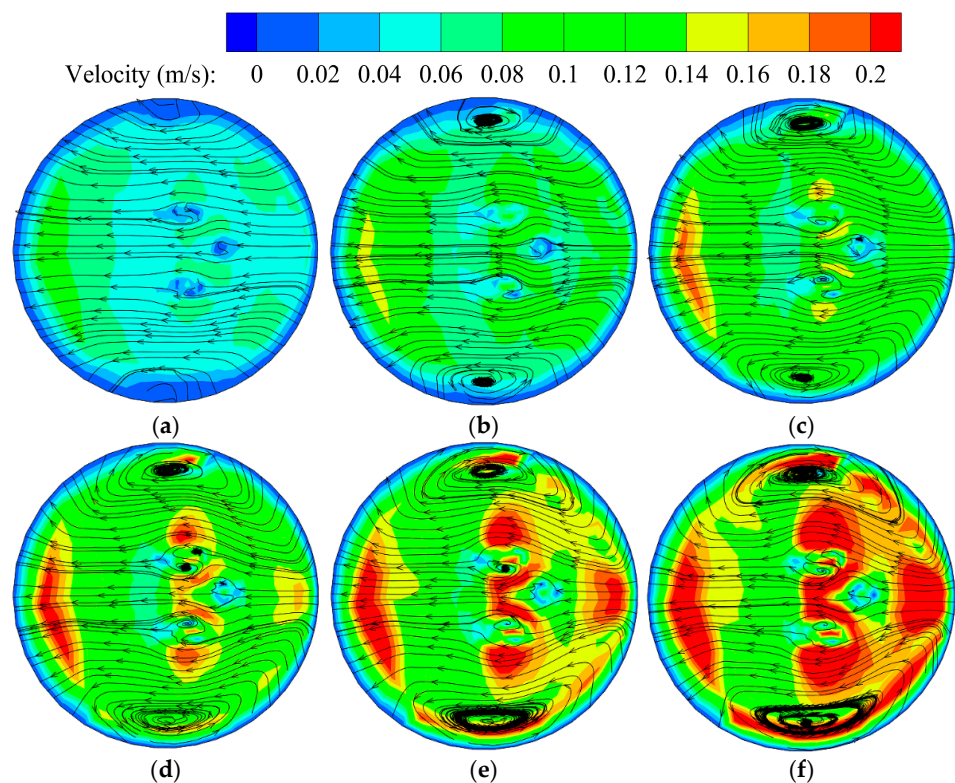


Figure 9. Cross-section A3 velocity and streamline distribution. (a) $0.33Q_d$, (b) $0.67Q_d$, (c) $1.00Q_d$, (d) $1.33Q_d$, (e) $1.67Q_d$, and (f) $2.00Q_d$.

Cross-section A4 flow velocity and streamline distribution is shown in Figure 10. It can be obtained from Figure 10 that the water flow in the inlet and outlet pipes is a high-speed zone, and under the low flow condition, there are vortices on the upper and lower sides of the inlet, and there are many small vortices at the upper and lower sides of the outlet. Under the high flow condition, the velocity at the water inlet decreases in a gradient toward the center of the prefabricated barrel, and the vortex at the water inlet moves toward the center. The vortex on the upper side of the prefabricated barrel inlet is gradually smaller than the vortex on the lower side, and the velocity and streamline in the prefabricated barrel are more chaotic. From the analysis of the change in working conditions, with the increase in flow rate, the velocity of water at the inlet is accelerated, and the vortex structure at the inlet becomes larger and pushes it to move to the center continuously, which affects the flow field at the center of the prefabricated barrel. Analysis from the position of, due to the influence of the flange structure, the flow of water above the outlet pipe is disturbed, and the vortex is generated.

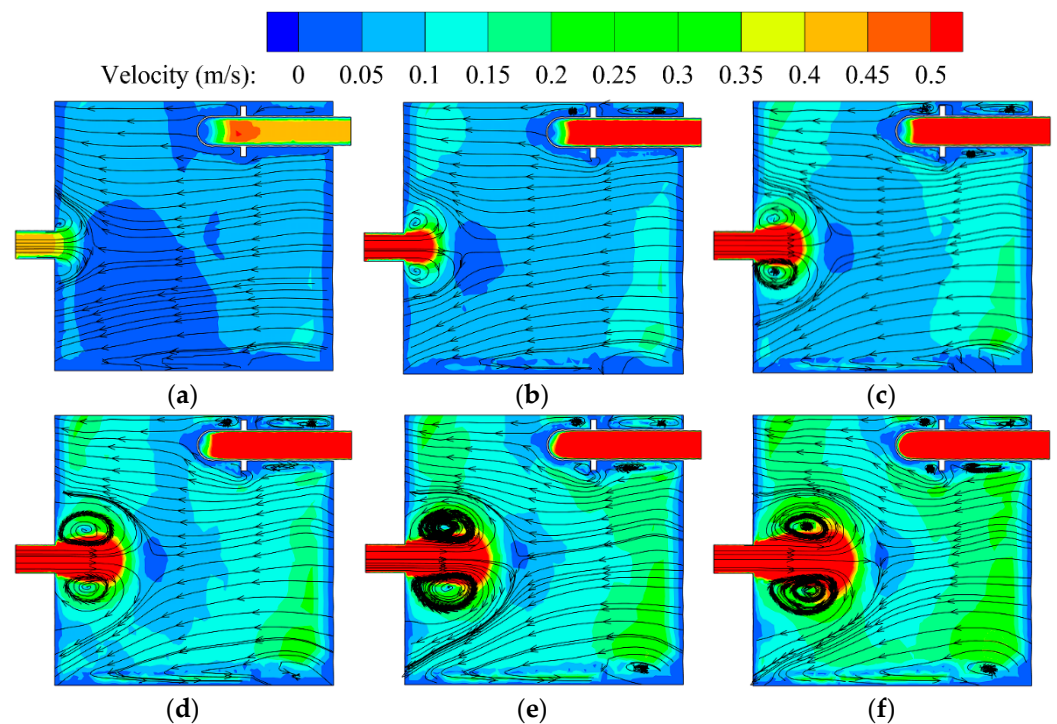


Figure 10. Cross-section A4 velocity and streamline distribution. (a) $0.33Q_d$, (b) $0.67Q_d$, (c) $1.00Q_d$, (d) $1.33Q_d$, (e) $1.67Q_d$, and (f) $2.00Q_d$.

Prefabricated pumping station wall pressure distribution is shown in Figure 11. From Figure 11, the pressure on the inlet side of the prefabricated barrel of the prefabricated pumping station gradually decreases with the increase in the flow rate until the maximum flow rate of $2.00Q_d$; only a small part of the high-pressure area exists on the upper side of the inlet and the upper side of the prefabricated barrel. Prefabricated pumping station prefabricated barrel outlet side pressure with the flow rate increases, the low-pressure area gradually decreases; until the maximum flow rate of $2.00Q_d$, the low-pressure area basically does not exist. In the centrifugal pump outlet connection pipeline, with the increase in flow, the low-pressure area becomes larger, mostly concentrated in the elbow of the double pump sink pipe. As the flow rate increases, the low-pressure area also appears on the waterward side of the centrifugal pump motor. Prefabricated barrel pressure distribution is not uniform, mainly in the inlet and outlet side is not consistent, along the inlet and outlet water axis, the symmetry of the left and right sides is slightly better, but also not completely symmetrical, can also be found in the phenomenon of partial flow.

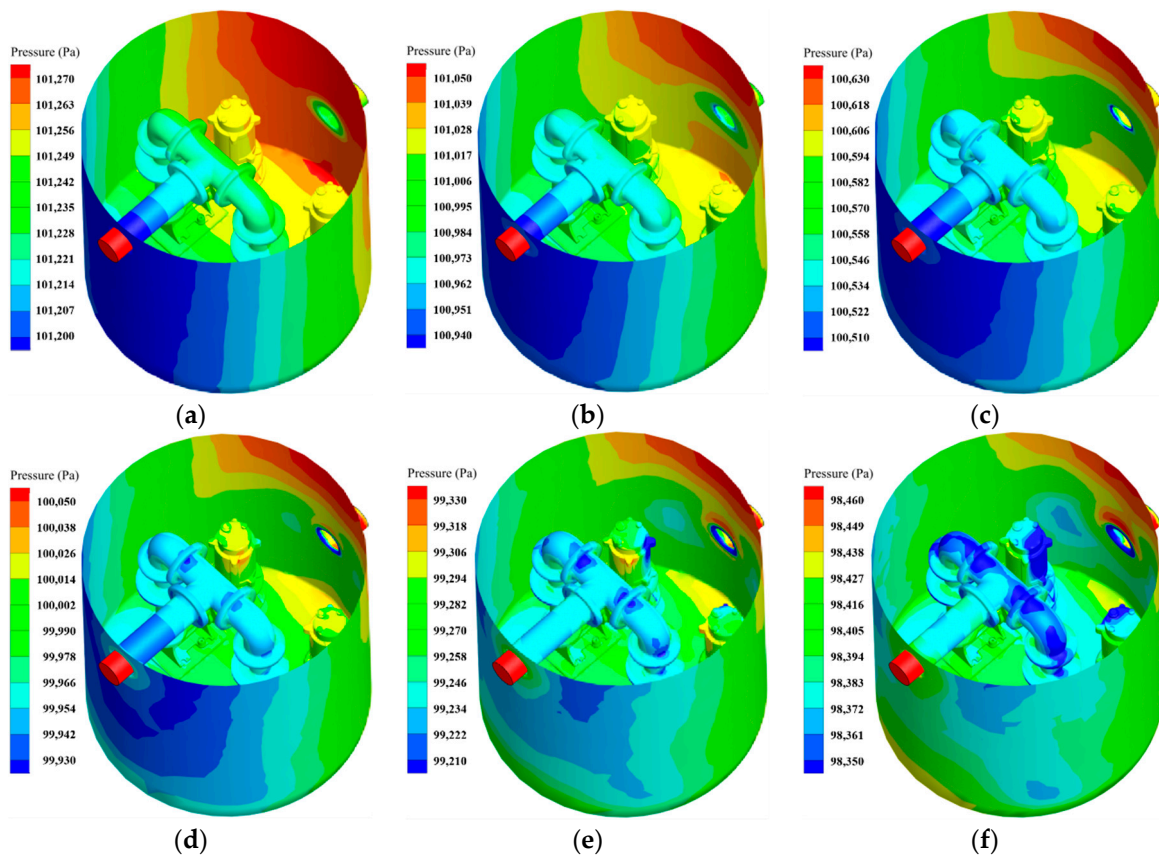


Figure 11. Prefabricated pumping station wall pressure distribution diagram. (a) $0.33Q_d$, (b) $0.67Q_d$, (c) $1.00Q_d$, (d) $1.33Q_d$, (e) $1.67Q_d$, and (f) $2.00Q_d$.

4. Experiment Equipment, Test and Result Analysis

4.1. Test Bench Introduction

Centrifugal prefabricated pumping station test bench has the following parts: Round prefabricated barrel, Back-flow tank, Submersible centrifugal pump, Coupler, Inlet and Outlet pipes, Electromagnetic Flow meter, Pipeline pump, and PLC frequency control cabinet. The total length of the test bench is about 5 m, the diameter of the pipe is 100 mm, and the whole is a circulating system. The whole test bench is made of acrylic material to achieve transparent visualization and to be able to clearly observe the flow pattern of water inside the centrifugal pumping station. Figure 12 shows the sketch of the centrifugal prefabricated pumping station test bench, Figure 13 shows the three-dimensional model of the centrifugal prefabricated pumping station test bench, and Figure 14 shows the physical drawing of the centrifugal prefabricated pumping station test bench. The flow rate is measured by an electromagnetic flowmeter (ZEF-DN100, range $0\sim 120\text{ m}^3/\text{h}$, accuracy $\pm 0.5\%$), and the flow pattern is captured by a high-speed camera (OLYMPUS i-SPEED 3, working range 2000 fps full resolution, accuracy $\pm 1\ \mu\text{s}$).

In this test, the centrifugal pump 3 was first adjusted to the rated speed $n = 2900\text{ r/min}$, and then the flow rate of the inlet of the prefabricated pumping station was adjusted to the design flow rate ($Q_d = 33.93\text{ m}^3/\text{h}$) by controlling the pipeline pump 6, and then the high-speed camera was used to take pictures of the internal flow state of the integrated, prefabricated pumping station.

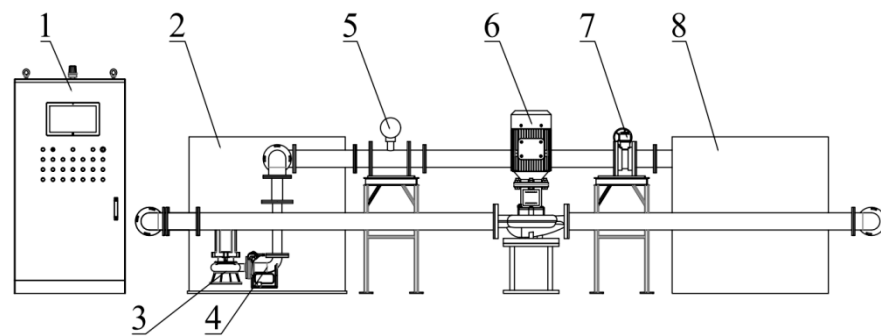


Figure 12. Sketch of centrifugal prefabricated pumping station test bench. 1. PLC variable frequency control cabinet; 2. round prefabricated barrels; 3. submersible centrifugal pump; 4. couplers; 5. electromagnetic flowmeter; 6. pipe pump; 7. turbo butterfly valve; 8. backflow tank.

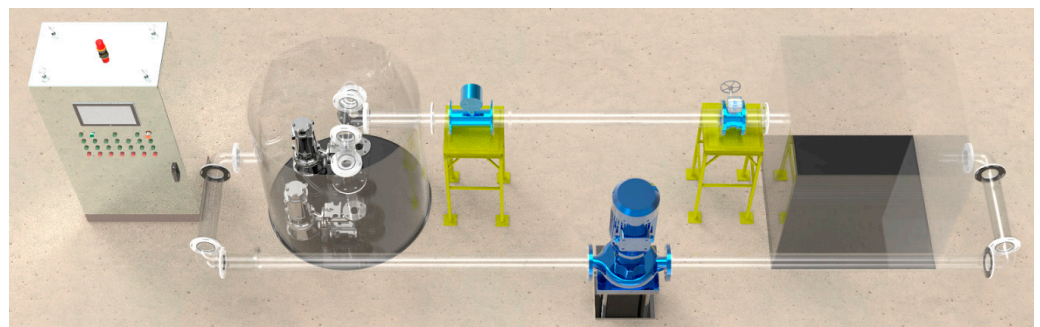


Figure 13. Three-dimensional model of centrifugal prefabricated pumping station.



Figure 14. Physical drawing of centrifugal prefabricated pumping station test bench.

4.2. Analysis of Experimental Results

In this paper, a high-speed camera is used to photograph the internal flow pattern of the prefabricated barrel under the design flow condition ($Q_d = 33.93 \text{ m}^3/\text{h}$), and a tracer red line is used to show the water flow to obtain pictures of the internal flow of the centrifugal prefabricated pumping station at different moments under different orientations.

Flow pattern of prefabricated pumping station. is shown in Figure 15. From Figure 15, it can be seen that the tracer line on both sides of the barrel wall oscillates with the flow of water. The direction of oscillation is from the outlet to the inlet, which is consistent with the direction of streamline in the numerical calculation results. At the intake, the tracer line can be seen to swirl with the water flow on both sides, which indicates that there is a backflow at the intake, and a vortex is generated. The internal flow characteristics are similar to those of the numerical calculation; the experimental study of flow pattern visualization is a verification of the numerical calculation results. The large variation in the position of the tracer red line under different moments and the large oscillation also indicate the

turbulence of the flow pattern in the prefabricated barrel of the centrifugal prefabricated pumping station and the inconsistency of the flow line.

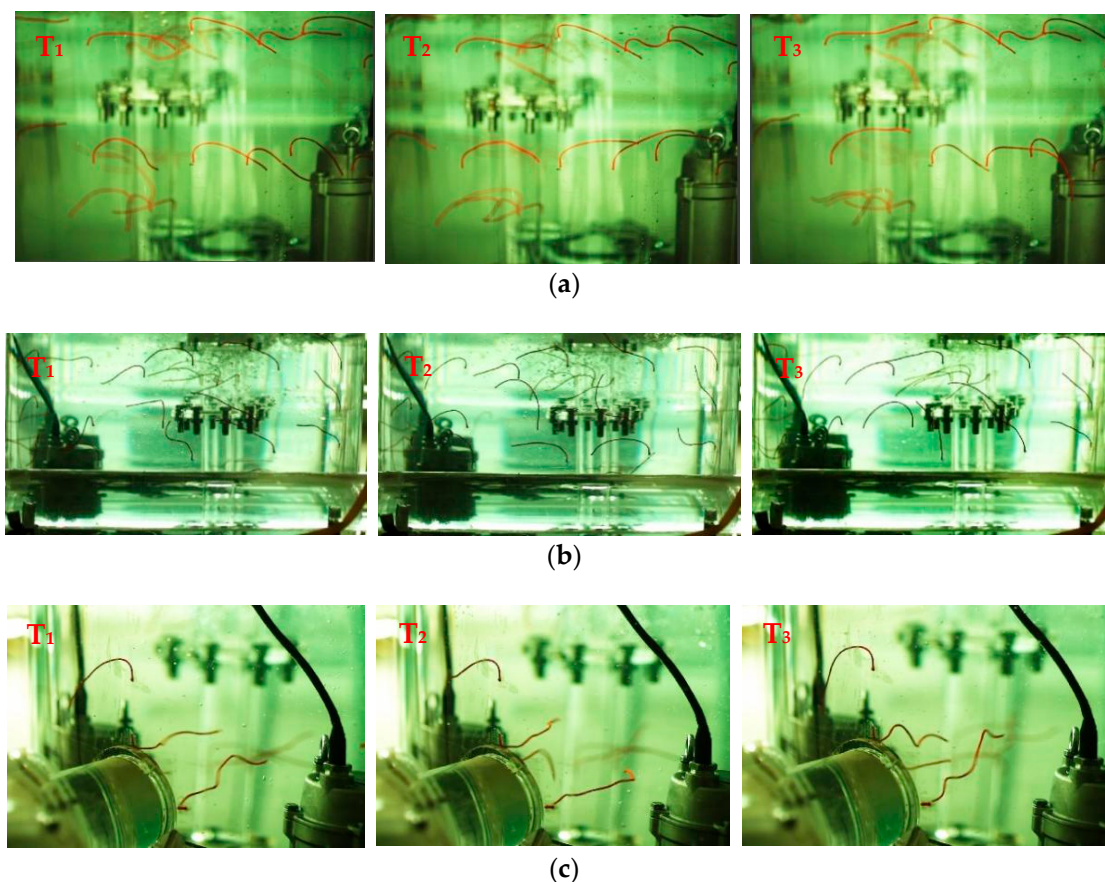


Figure 15. Flow pattern of prefabricated pumping station. (a) Left side of prefabricated barrel; (b) right side of prefabricated barrel; (c) filming at the inlet of the prefabricated barrel.

5. Conclusions

This paper takes centrifugal prefabricated pumping station as the research object; numerical calculation of different working conditions under double pumping operation conditions and analysis and discussion of internal flow characteristics of prefabricated pumping station are carried out. An acrylic visualization prefabricated pumping station test bench was built to verify the numerical calculation results of centrifugal prefabricated pumping station by experimentally filming the internal flow pattern of the prefabricated pumping station, and the main conclusions are as follows.

(1) The calculation shows that the maximum value is reached at the design working condition ($Q_d = 33.93 \text{ m}^3/\text{h}$); the maximum efficiency value is 63.96%; the head is 8.66 m; the head at the starting point of the saddle area is 10.50 m, which is 1.21 times of the design head; the operable head range for small flow is small; and the operable head range for large flow is wide. The efficiency of the prefabricated pumping station in the high-efficiency zone is 58.0~63.0%, corresponding to the flow range of $0.62Q_d \sim 1.41Q_d$ ($21.0 \sim 48.0 \text{ m}^3/\text{h}$).

(2) Through the numerical calculation, it can be obtained that the impeller inlet flow uniformity increases with the increase in flow rate, and it is basically maintained at the same value from $0.83Q_d$ to $2.33Q_d$. The impeller inlet flow uniformity of pump 2 is greater than that of pump 1. At the design working condition ($Q_d = 33.93 \text{ m}^3/\text{h}$), the impeller inlet flow uniformity of pump 1 is 74.70%, and that of pump 2 is 75.57%. The inlet flow fields of the pumps on both sides are not consistent. When the flow condition is less than $0.83Q_d$ ($Q = 28.27 \text{ m}^3/\text{h}$), the uniformity of flow velocity at the impeller inlet increases significantly and cannot provide a better impeller inlet flow pattern.

(3) Through the numerical calculation of velocity and pressure cloud diagrams as well as the experimental flow analysis, it can be obtained that the centrifugal prefabricated pumping station has a serious backflow phenomenon at the inlet, and multiple vortexes are generated. As the flow rate increases, the vortex structure at the inlet expands and moves to the central area, which has a negative impact on the flow field in the central area. The flow pattern in the prefabricated barrel was unstable, and there was a partial flow on the left and right sides.

6. Suggestions

This paper reveals the energy characteristics and internal flow field of centrifugal prefabricated pumping stations under double pump operation conditions through numerical calculation and experimental analysis. However, because of the limited page, the research work has achieved certain results, but there are still many problems that can be studied and need to be further expanded and deepened in future work. In the future, we will start the multi-disciplinary optimization design of centrifugal prefabricated pumping station with multiple working conditions, and the research results of this paper can provide the basis for the optimization design of centrifugal prefabricated pumping station.

Author Contributions: Concept design, C.X. and Z.Y.; Numerical calculation, Z.Y., A.F. and Z.W.; Experiment and data analysis, Z.Y., A.F., Z.W. and L.W.; Manuscript writing, C.X. and Z.Y. All authors have read and agreed to the published version of the manuscript.

Funding: This research was funded by Anhui Province Natural Science Funds for Youth Fund Project, grant number 2108085QE220. Key scientific research project of Universities in Anhui Province, grant number KJ2020A0103. Anhui Province Postdoctoral Researchers' Funding for Scientific Research Activities, grant number 2021B552. Anhui Agricultural University President's Fund, grant number 2019zd10. Stabilization and Introduction of Talents in Anhui Agricultural University Research Grant Program, grant number rc412008.

Institutional Review Board Statement: Not applicable.

Informed Consent Statement: Not applicable.

Data Availability Statement: Not applicable.

Conflicts of Interest: The authors declare no conflict of interest.

References

1. Wang, D. Research on design development and application of integrated prefabricated pumping station. *Gen. Mach.* **2014**, *7*, 87–88.
2. Fang, A.B. Research and application of integrated drainage pumping station. *Build. Mater. Decor.* **2020**, *1*, 218–219.
3. Zhang, Z.; Wang, K.; Chen, K.; Yang, J.; Wang, S.; Wang, Y. Effects of different operation modes on flow characteristics and cylinder strength of integrated prefabricated pumping stations. *China Rural. Water Conserv. Hydropower* **2019**, *4*, 162–167.
4. Li, Q.; Kang, C.; Teng, S.; Li, M. Optimization of Tank Bottom Shape for Improving the Anti-Deposition Performance of a Prefabricated Pumping Station. *Water* **2019**, *11*, 602.
5. Wang, K.; Hu, J.; Liu, H.; Zhang, Z.; Zou, L.; Lu, Z. Research on the Deposition Characteristics of Integrated Prefabricated Pumping Station. *Symmetry* **2020**, *12*, 760. [[CrossRef](#)]
6. Zhang, B.; Cheng, L.; Xu, C.; Wang, M. The Influence of Geometric Parameters of Pump Installation on the Hydraulic Performance of a Prefabricated Pumping Station. *Energies* **2021**, *14*, 1039. [[CrossRef](#)]
7. Iacob, N.; Drăgan, N. Dynamic Analysis of a Centrifugal Pump using CFD and FEM Methods. *Hidraulica* **2019**, *4*, 29–37.
8. Ramakrishna, R.; Hemalatha, S.; Rao, D.S. Analysis and performance of centrifugal pump impeller. *Mater. Today Proc.* **2022**, *50*, 5. [[CrossRef](#)]
9. Kumar, S.V.; Han, X.; Kang, Y.; Li, D.; Zhao, W.; Selamat, F.E.; Wan Izhan, W.H.I.; Baharudin, B.S.; Bellary, S.A.I. Upgradation in efficiency of centrifugal pump. *Asian J. Multidimens. Res.* **2021**, *10*, 32–34.
10. Tong, Z.; Xin, J.; Tong, S.; Yang, Z.; Zhao, J.; Mao, J. Internal flow structure, fault detection, and performance optimization of centrifugal pumps. *J. Zhejiang Univ.-Sci. A Appl. Phys. Eng.* **2020**, *21*, 85–117. [[CrossRef](#)]
11. Al-Obaidi, A.R. Numerical investigation on effect of various pump rotational speeds on performance of centrifugal pump based on CFD analysis technique. *Int. J. Modeling Simul. Sci. Comput.* **2021**, *12*, 2150045. [[CrossRef](#)]
12. Shunya, T.; Shinichi, K.; Shinichiro, E.; Masahiro, M. Effect of diffuser vane slit on rotating stall behavior and pump performance in a centrifugal pump. *J. Phys. Conf. Ser.* **2022**, *2217*, 012054.

13. Tan, M.; Lu, Y.; Wu, X.; Liu, H.; Tian, X. Investigation on performance of a centrifugal pump with multi-malfunction. *J. Low Freq. Noise Vib. Act. Control* **2020**, *40*, 740–752. [[CrossRef](#)]
14. Susilo, S.H.; Setiawan, A. Analysis of the number and angle of the impeller blade to the performance of centrifugal pump. *EUREKA Phys. Eng.* **2021**, *5*, 62–68. [[CrossRef](#)]
15. Ding, H.; Li, Z.; Gong, X.; Li, M. The influence of blade outlet angle on the performance of centrifugal pump with high specific speed. *Vacuum* **2019**, *159*, 239–246. [[CrossRef](#)]
16. Lila, A.; Mathieu, S.; Idir, B.; Smaïne, K. Numerical Assessment of the Hydrodynamic Behavior of a Volute Centrifugal Pump Handling Emulsion. *Entropy* **2022**, *24*, 221. [[CrossRef](#)]
17. Deepak, M.; Tony, K.; Atma, P.; Sajid, A.; Faik, H. Effect of Geometric Configuration of the Impeller on the Performance of Liquivac Pump: Single Phase Flow (Water). *Fluids* **2022**, *7*, 45. [[CrossRef](#)]
18. Yu, T.; Shuai, Z.; Jian, J.; Wang, X.; Ren, K.; Dong, L.; Li, W.; Jiang, C. Numerical study on hydrodynamic characteristics of a centrifugal pump influenced by impeller-eccentric effect. *Eng. Fail. Anal.* **2022**, *138*, 106395. [[CrossRef](#)]
19. Elyamin, G.R.H.A.; Bassily, M.A.; Khalil, K.Y.; Gomaa, M.S. Effect of impeller blades number on the performance of a centrifugal pump. *Alex. Eng. J.* **2019**, *58*, 39–48. [[CrossRef](#)]
20. Zhaoheng, L.; Fangfang, Z.; Faye, J.; Ruofu, X.; Ran, T. Influence of the hydrofoil trailing-edge shape on the temporal-spatial features of vortex shedding. *Ocean. Eng.* **2022**, *246*, 110645.
21. Menter, F.R. Zonal two equation $k-\omega$ turbulence models for aerodynamic flows. In Proceedings of the 23rd Fluid Dynamics, Plasmadynamics, and Lasers Conference, Orlando, FL, USA, 6–9 July 1993; p. 2906.
22. Lu, Z.; Xiao, R.; Tao, R.; Li, P.; Liu, W. Influence of guide vane profile on the flow energy dissipation in a reversible pump-turbine at pump mode. *J. Energy Storage* **2022**, *49*, 104161. [[CrossRef](#)]
23. Fang, X.; Hou, Y.; Cai, Y.; Chen, L.; Lai, T.; Chen, S. Study on a high-speed oil-free pump with fluid hydrodynamic lubrication. *Adv. Mech. Eng.* **2020**, *12*, 1687814020945463. [[CrossRef](#)]
24. Stuparu, A.; Baya, A.; Bosioc, A.; Anton, L.; Mos, D. Experimental investigation of a pumping station from CET power plant Timisoara. *IOP Conf. Ser. Earth Environ. Sci.* **2019**, *240*, 032018. [[CrossRef](#)]
25. Hassan, S.M.; Salman, S. Effects of impeller geometry modification on performance of pump as turbine in the urban water distribution network. *Energy* **2022**, *255*, 124550.
26. Liu, Y.; Xia, Z.; Deng, H.; Zheng, S. Two-Stage Hybrid Model for Efficiency Prediction of Centrifugal Pump. *Sensors* **2022**, *22*, 4300. [[CrossRef](#)] [[PubMed](#)]
27. Francesco, P.; Maurizio, G. An Operative Framework for the Optimal Selection of Centrifugal Pumps As Turbines (PATs) in Water Distribution Networks (WDNs). *Water* **2022**, *14*, 1785.
28. Parkes, A.I.; Sobey, A.J.; Hudson, D.A. Physics-based shaft power prediction for large merchant ships using neural networks. *Ocean. Eng.* **2018**, *166*, 92–104. [[CrossRef](#)]
29. Wang, X.; Zhang, J.; Li, Z. Numerical Simulation of Internal Flow Field of Self-Designed Centrifugal Pump. In Proceedings of the 2021 International Conference on Fluid and Chemical Engineering (ICFCE 2021), Wuhan, China, 29–30 October 2021; pp. 158–166.
30. Sun, Z.; Yu, J.; Tang, F. The Influence of Bulb Position on Hydraulic Performance of Submersible Tubular Pump Device. *J. Mar. Sci. Eng.* **2021**, *9*, 831. [[CrossRef](#)]